



Oscillating non-progressing flows induce directed cell motion

Winfried Schmidt ^{1,2}, Andre Förtsch,¹ Matthias Laumann,¹ and Walter Zimmermann ^{1,*}

¹*Theoretische Physik, Universität Bayreuth, 95440 Bayreuth, Germany*

²*Laboratoire Interdisciplinaire de Physique, Université Grenoble Alpes and CNRS, F-38000 Grenoble, France*



(Received 4 October 2021; accepted 18 February 2022; published 16 March 2022)

We present a deformation-dependent propulsion phenomenon for soft particles such as cells in microchannels. It is based on a broken time-reversal symmetry generated by a fast forward and a slow backward motion of a fluid which does not progress on average. In both sections, soft particles deform differently and thus progress relatively to the liquid. We demonstrate this by using Lattice-Boltzmann simulations of ubiquitous red blood cells in microchannels, as well as simulations for capsules and minimal-soft-tissue models in unbounded Poiseuille flows. The propulsion of the soft particles depends besides the oscillation asymmetry on their size, deformation type, and elasticity. This is also demonstrated by analytical calculations for a minimal model. Our findings may stimulate a rethinking of particle sorting methods. For example, healthy and malignant cells often differ in their elasticity. With the proposed method, several cell types with different deformabilities can be separated simultaneously without labeling or obstacles in a microfluidic device.

DOI: [10.1103/PhysRevFluids.7.L032201](https://doi.org/10.1103/PhysRevFluids.7.L032201)

The massive growth of the field of microfluidics is due to a number of recent advances, including methods for focusing and sorting microparticles, such as healthy and cancerous cells [1–12]. In particular, label-free hydrodynamic separation methods are finding increasing applications due to their robustness. Here, we report on a microfluidic transport process based on symmetry breaking and appropriate for separation of particles of different elasticities, such as healthy from diseased cells.

The change in deformability of individual cells has proven to be a useful indicator for the detection of diseases such as cancer [13,14], blood diseases (sickle cell anemia) [15], inflammation [16], malaria [17], and diabetes [18]. In particular, the stiffness of individual cancer cells is drastically reduced compared to normal tissue of the same origin. Furthermore, decreasing single cell stiffness correlates with increasing invasiveness or metastatic potential. From this perspective, there is a great need for methods to safely separate cells of different stiffnesses.

The widely used microfluidic particle separation methods such as filtration [19], inertial microfluidics, including curved microchannels [9,20], and deterministic lateral displacement (DLD) [21–24] are successful methods especially for separating solid particles of different sizes. For these classical separation techniques the deformability of particles is an additional degree of freedom and ongoing research is addressing the associated effects [24,25].

In contrast, several transport phenomena in low-Reynolds-number microfluidics only occur for soft particles. This is the lift force of vesicles and capsules in linear shear flows and Poiseuille flows near symmetry-breaking walls [26–29]. In Poiseuille flows, the shear rate changes across deformable particles and breaks their forward-backward symmetry, so that droplets [30,31], bubbles, and capsules [32–34] even in unconfined Poiseuille flows exhibit cross-stream migration (CSM)

*Corresponding author: walter.zimmermann@uni-bayreuth.de

toward the center of a parabolic flow profile. The CSM direction is reversed by a sufficiently strong viscosity contrast between the interior of cells and the surrounding fluid [35] or in vertical channels for non-buoyant capsules by gravitational effects [36]. For modulated microchannels, a secondary attractor occurs aside from the channel center for soft particles such as red blood cells (RBCs) and capsules [37]. These examples for CSM are, however, not appropriate to separate particles with respect to a continuous variation of deformability.

Time-periodic flows in microchannels have increasingly attracted attention [38–48]. Among others, they are utilized in combination with arrays of asymmetric posts in microchannels to realize deterministic ratchets [41] or to reduce clogging in DLD arrays by particles [42,43].

We complement time-periodic flows with a crucial symmetry breaking. This is achieved by different forward and backward velocities of a fluid in the microchannel that does not move on average. We study four types of soft particles that are deformed and entrained differently during the two sections of the low-Reynolds-number flow. As a consequence, deformable particles are propelled relative to the fluid. This net transport increases with asymmetry of the flow oscillation, particle deformability, and size. Thus, our propulsion mechanism is suitable for the development of promising deformation-sensitive cell sorting methods.

The pulsating, undisturbed flow between the plane channel boundaries at $y = \pm w$ is given by

$$\mathbf{u}(\mathbf{r}, t) = \tilde{u}(t) \left(1 - \frac{y^2}{w^2}\right) \hat{e}_x, \quad (1)$$

with the unit vector \hat{e}_x in the x direction. We consider a rectangular time dependence,

$$\tilde{u}(t) = \begin{cases} u_1 > 0 & \text{for } t \in [0, T_1[, \\ u_2 < 0 & \text{for } t \in [T_1, T[, \end{cases} \quad (2)$$

repeating periodically with the flow period $T = T_1 + T_2$. For non-progressing flows the velocities $u_{1,2}$ are related to the time intervals $T_{1,2}$ via

$$u_1 T_1 + u_2 T_2 = 0 \Leftrightarrow A = \frac{T_2}{T_1} = -\frac{u_1}{u_2}, \quad (3)$$

with the oscillation asymmetry A . The time-dependent flow amplitude $\tilde{u}(t)$ is sketched in Fig. 1(a) for $A = 2$.

We consider four types of soft particles. The minimal model (MM), the two-dimensional (2D) ring polymer, and the 3D capsule are represented by N beads with radius a . The MM consists of three beads connected by three Hookean springs with the spring constant k and equilibrium lengths b and $2b$. It is perpendicularly oriented to \hat{e}_x . The ring polymer model is represented by a closed bead-spring chain with ten beads placed in the x - y (shear) plane. They are connected by Hookean springs, and a bending potential [49] along the chain provides a ring shape in the quiescent liquid. The capsule is built of a triangular mesh where the beads are situated at the $N = 642$ nodes. We use the Neo-Hookean law [50] for the strain energy with the surface shear-elastic modulus κ_S and a bending potential [51] with the bending rigidity κ_B . A volume potential [52] with the volume modulus κ_V penalizes deviations from the reference volume $V_0 = 4\pi r_0^3/3$ of the capsule's spherical initial shape with the radius r_0 . The center of each particle is at $\mathbf{r}_c = \sum_{i=1}^N \mathbf{r}_i/N$, with bead positions $\mathbf{r}_i = (x_i, y_i, z_i)$. The Stokesian dynamics of the beads is described by

$$\dot{\mathbf{r}}_i = \mathbf{u}(\mathbf{r}_i, t) + \sum_{j=1}^N \mathbf{H}_{ij} \cdot \mathbf{F}_j. \quad (4)$$

The forces acting on the beads are $\mathbf{F}_j = -\nabla_j E(\mathbf{r})$, with the total particle-specific potential $E(\mathbf{r})$ as described above and \mathbf{H}_{ij} being the mobility matrix [53–55]. Particle-wall interactions are neglected.

The RBC consists of a mesh with the same refinement as the capsule, but has a biconcave initial shape. The strain energy is modeled by the Skalak law [52,56] with the strain modulus κ_S and the

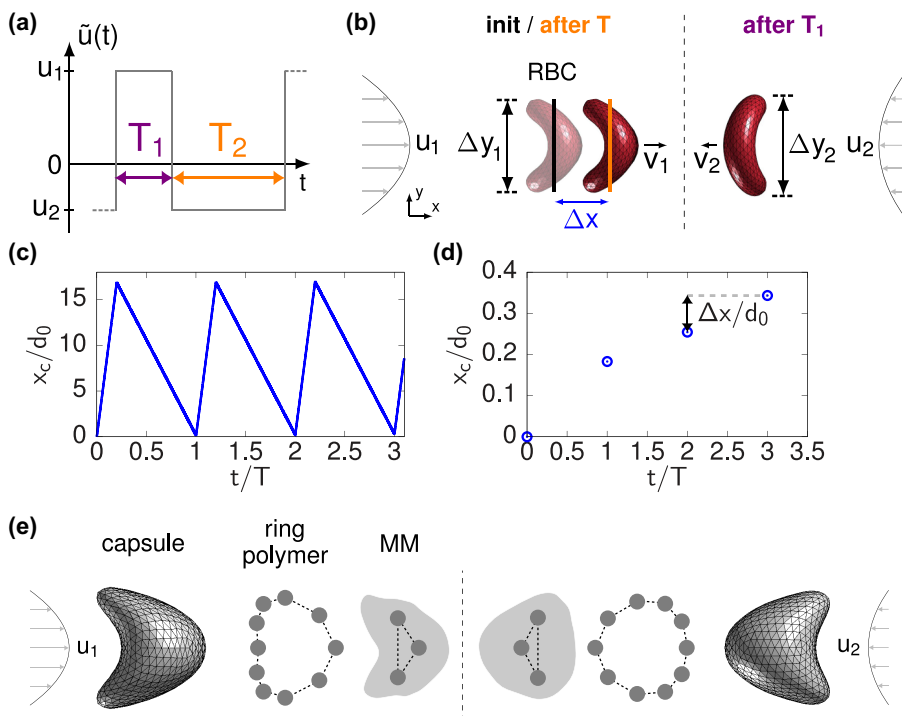


FIG. 1. (a) Time dependence of $\tilde{u}(t)$ with time intervals T_1 (forward flow, purple) and T_2 (backward flow, orange) and asymmetry $A = T_2/T_1 = 2$. (b) Different RBC shapes during the faster forward and slower backward flow with $u_1 > |u_2|$, different lateral sizes $\Delta y_1 < \Delta y_2$, and velocities $v_1 > |v_2|$. The resulting net progress Δx (blue) per flow period $T = T_1 + T_2$ is the difference between the RBC's initial position (shaded snapshot, black bar) and its final position (bold snapshot, orange bar). (c) RBC position $x_c(t)$ along the channel axis in units of its undeformed diameter d_0 obtained by a LBM simulation as a function of time for three asymmetric flow cycles with $A = 4$. (d) Local minima of $x_c(t)$ with the propulsion step Δx . (e) Simulation snapshots for the capsule, the ring polymer, and the minimal model during the forward flow section (left) and the backward flow section (right).

area dilation modulus κ_α . A bending potential according to Ref. [57] is used and volume conservation is implemented as for the capsule. The RBC's initial orientation is chosen so that the rotational symmetry axis of its initial shape is parallel to the flow direction. For simulations of the RBC we use the Lattice-Boltzmann method (LBM) with the Bhatnagar-Gross-Krook collision operator and the immersed-boundary method [58–60]. The LBM inherently accounts for hydrodynamic interactions (HIs) of particles with the channel boundaries. For more information on simulation methods and particle models, see Ref. [61]. If not stated otherwise, the simulation parameters in Ref. [62] are used.

Figure 1(b) shows simulation snapshots of the RBC with typical croissantlike shapes [63] during the faster forward and the slower backward flow. The two different deformations of the RBC are characterized by the vertical extensions $\Delta y_{1,2}$. This leads to different particle velocities along the channel axis, $v_1 > 0$ and $v_2 < 0$, with $v_1 \neq |v_2|$. Despite vanishing mean flow, the RBC is propelled after each flow cycle by a step $\Delta x > 0$. The RBC's x position is shown as a function of time in a pulsatile flow with $A = 4$ in Fig. 1(c). The particle follows the flow alternately in the positive x direction and the negative x direction, with the nonzero propulsive step relative to the liquid shown in Fig. 1(d). Figure 1(e) shows the corresponding snapshots for the capsule, the ring polymer, and the MM.

The flow-induced deformation of a particle depends essentially on the curvature of the flow profile in Eq. (1), the particle size, the liquid viscosity, and the particle elasticity. These dependencies can be summarized by the dimensionless capillary number

$$C = \frac{2|\tilde{u}|r_0t_R}{w^2}, \quad (5)$$

with $C = C_{1,2}$ in the two flow sections $T_{1,2}$. Here, $2|\tilde{u}|/w^2 = |\partial_y^2 u_x(y, t)|$ is the curvature of a plane Poiseuille flow and $2r_0 = d_0$ is the initial diameter of the particle. For the MM, $d_0 = 2b$ holds and for the RBC d_0 refers to the large diameter of its initial biconcave shape. The particle's relaxation time is given by $t_R = \zeta/k$ for the MM and the ring polymer and by $t_R = \eta r_0/\kappa_S$ for the capsule and the RBC, where $\zeta = 6\pi\eta a$ is the Stokes friction and η is the fluid viscosity. The particle deformation depends also on hydrodynamic particle-wall interactions, but they provide only corrections to the leading-order bulk effect as shown below for the RBC.

The RBC and the MM in Fig. 1 adapt a curved shape that is induced by the y dependence of $u_x(y, t)$ and the associated frictional forces acting on the particle. Therefore, as the capillary number C increases, the RBC and the MM become more curved, which in turn leads to a decrease in the vertical extension, i.e., $\Delta y_1 < \Delta y_2 < d_0$. The particle velocity v results from an averaging of the local incident flow velocity over the particle surface. Accordingly, an increasing C results in a decreasing averaging length Δy and, therefore, in an increasing ratio v/\tilde{u} . In other words, the particle's lag behind with respect to the incident flow at its center is smaller in the forward section than in the backward section. Thus, $v_1/\tilde{u}_1 > |v_2/\tilde{u}_2|$ and the propulsion step $\Delta x = v_1T_1 + v_2T_2$ is positive.

In the limit of small deformations, the quantities Δx and Δy can be determined analytically in terms of the particle properties for the MM. The velocities $v_{1,2}$ determine the propulsion velocity according to

$$v_p = \frac{\Delta x}{T} = \frac{v_1 + Av_2}{A + 1}. \quad (6)$$

With the explicit expressions for v_1 and v_2 (see Supplemental Material [61]), the propulsion velocity is given by

$$v_p \approx \frac{b}{3t_R} B_1 \frac{W(A)A^{\frac{1}{3}} - W(1)}{A + 1}, \quad (7)$$

with $W(X) = \sqrt{1 + 8X^{\frac{2}{3}}(4X^{\frac{2}{3}} + B_1)^{-1}}$ and $B_{1,2} = (2C_{1,2}^2)^{1/3}$. The vertical extension Δy of the MM decreases with increasing C at leading order in the following manner:

$$\Delta y_{1,2} \approx 2b \left[1 - \frac{B_{1,2}}{12} + O(B_{1,2}^2) \right]. \quad (8)$$

For a symmetric flow pulsation one has $\tilde{u}_1 = -\tilde{u}_2$ and thus $C_1 = C_2$. According to Eq. (8), the flow-induced deformation in the two flow sections is identical with $\Delta y_1 = \Delta y_2$. The shape is only mirrored after the change from the forward flow to the backward flow. That is, v_p vanishes for $A = 1$ according to Eq. (7). For $A \neq 1$, this mirror symmetry is broken, as shown in Fig. 1(e), and v_p becomes finite. As the asymmetry $A > 1$ increases, the difference in vertical extensions, $\Delta y_2 - \Delta y_1$, and v_p also increase. Moreover, the propulsive step increases with the capillary number C_1 and the particle size given by b , but decreases with t_R . If one changes the sign of $\tilde{u} \rightarrow -\tilde{u}$, the propulsive direction (sign of Δx) also changes.

Whereas the vertical extension of the MM and the RBC decreases with \tilde{u} , the lateral size of the capsule and the ring polymer increases with C . In Fig. 2(a) we show the evolution of the deformation of a capsule after a sudden onset of a stationary parabolic flow for the two values $C' = 0.98$ and $C'' = 0.49$. After a time of the order of t_R , the capsule's deformation reaches a stationary, bulletlike shape with a vertical extension larger than that in its undeformed state, i.e., $\Delta y' > \Delta y'' > d_0$. The corresponding snapshots are shown in Fig. 2(b). Similar deformations are found for stiffer cells

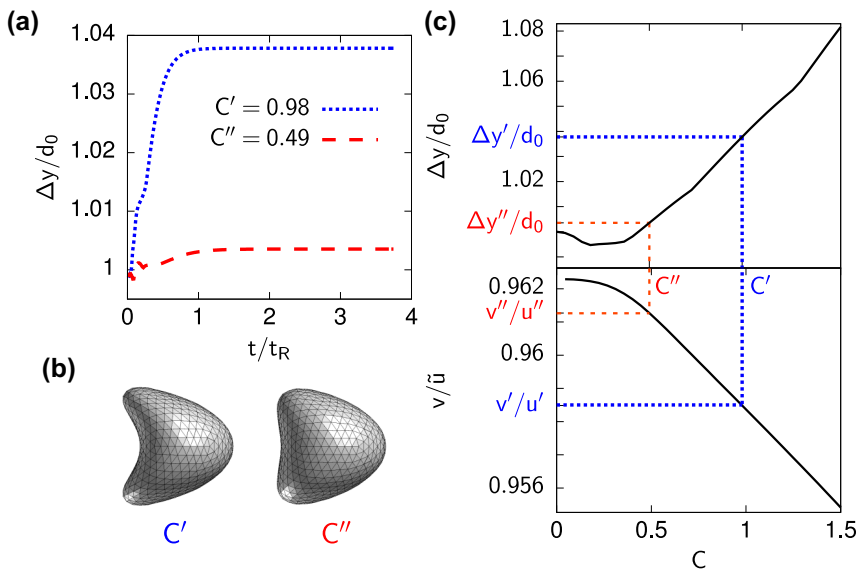


FIG. 2. Shape-dependent entrainment of capsules in stationary Poiseuille flow. (a) Time evolution of the capsule's lateral extension Δy after the onset of the flow at $t = 0$ for the two capillary numbers $C' = 0.98$ and $C'' = 0.49$. (b) Simulation snapshots of the capsule after the stationary shape is reached. (c) Plateau value of the lateral size [see (a)] (top) and relative velocity v/\bar{u} (bottom) as a function of the capillary number. Increasing Δy results in decreasing v/\bar{u} .

[64,65]. This increase in lateral size is in contrast to the RBC and in agreement with previous simulation results on capsules [66].

Note that any finite-sized particle in a parabolic flow profile lags behind \bar{u} ; i.e., $v/\bar{u} < 1$ always holds. Using the same reasoning as above, an increasing vertical extension Δy for capsules leads to a decreasing ratio v/\bar{u} , as shown in Fig. 2(c). In the asymmetrically oscillating flow as given in Eq. (1), this results in $v_1/\bar{u}_1 < |v_2/\bar{u}_2|$ and a negative propulsion step for the capsule and the ring polymer.

The determination of the evolution of a soft particle's deformation such as for the capsule in Fig. 2(a) gives the lower bounds of $T_{1,2}$ for a pulsating flow as well as the sign of Δx . $T_{1,2}$ should always be chosen significantly larger than t_R of a soft particle in order to obtain a reasonable difference between the traveled distances per flow section, $v_1 T_1$ and $|v_2| T_2$. Since $\Delta x \propto T$ according to Eq. (6), the total net progress after n oscillation cycles will be the same if T is increased and n is decreased proportionally, provided that $t_R \ll T_{1,2}$ applies.

The different sign and the dependence of Δx on C_1 is shown in Fig. 3 for three different particles. C_1 is changed by the flow amplitude \bar{u} in $T_{1,2}$ with $C_2 = C_1/A$ and $A = 2$. For all particles, the magnitude $|\Delta x|$ increases with growing C_1 . The analytical result according to Eq. (7) approximates the numerical results for the MM in Fig. 3 quite well, especially for small C_1 .

$|\Delta x|$ increases monotonically with A for all types of soft particles, as shown in Fig. 4. Starting from $A = 1$, we increase the flow asymmetry by lengthening T_2 and decreasing u_2 accordingly, while keeping T_1 and u_1 fixed. The analytical approximation [see Eq. (7)] and numerical calculations for the MM also agree well here.

So far our results for simulations in unbounded flows show that the net propulsion of soft particles in asymmetrically oscillating flows originates from a leading bulk contribution as the particle-wall HI has been neglected. This is a good approximation for the case of a small confinement parameter $\chi = d_0/(2w)$. In order to address the influence of the walls, we turn towards LBM simulations in the following. In Fig. 5 the propulsion step per flow period is shown as a function of the

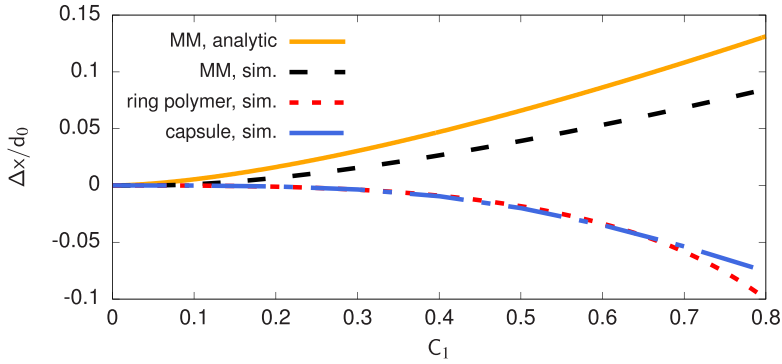


FIG. 3. Propulsion step Δx as a function of the capillary number of the forward flow section, C_1 , for different particles in unbounded flows: Capsule (blue long-dashed line), ring polymer (red short-dashed line), and minimal model (analytical: orange solid line; simulation: black dashed line). Δx is given in units of the respective initial particle diameters d_0 .

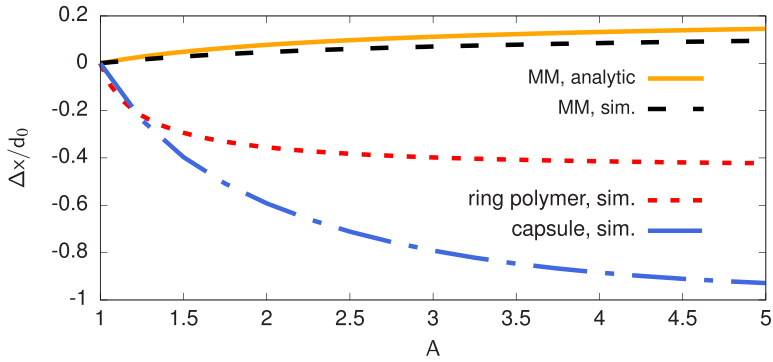


FIG. 4. Propulsion step Δx in units of the initial particle diameter d_0 as a function of the asymmetry of the oscillating flow, A , for the same particles as in Fig. 3.

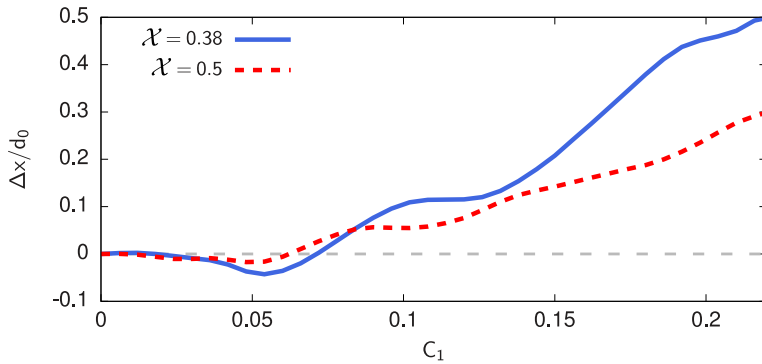


FIG. 5. Propulsion step Δx of a red blood cell in units of its initial diameter d_0 as function of the capillary number C_1 in the forward section of the asymmetrically oscillating flow. The results are obtained by Lattice-Boltzmann simulations (bounded flows) with a flow asymmetry $A = 4$ for two confinements $\chi = 0.38$ (solid line) and $\chi = 0.5$ (dashed line).

capillary number for a RBC in bounded Poiseuille flow with $A = 4$. The results for two different, experimentally common values of $\chi = 0.5$ and $\chi = 0.38$ are displayed. For the determination of Δx , we take the average value covering the range of three flow periods. For small C_1 , Δx becomes negative at first, similar to capsules. However, the propulsion step changes sign at intermediate values of C_1 and then continues to grow monotonically with C_1 . Nevertheless, the magnitude $|\Delta x|$ is larger for $\chi = 0.38$ than for $\chi = 0.5$ throughout the majority of values of the capillary number in Fig. 5. Therefore we conclude that the propulsive effect is reduced, but only quantitatively changed by the particle-wall HI. For a multiparticle simulation we refer to Ref. [61]. Our results are confirmed by recent experiments on RBCs in pulsating flows [67].

In this work, we identified and described a propulsion mechanism for soft particles in microchannels. In contrast to so-called microfluidic deterministic ratchets [41–43] it does not rely on asymmetric posts in microchannels for directed particle motion in pulsating flows. Rather, time-reversal symmetry is broken by using different forward and backward velocities of an on average non-progressing liquid. Since soft particles are deformed and entrained differently in the two flow sections, they are selectively propelled according to their deformability, whereas rigid particles do not move on average.

The propulsion direction of a soft particle in pulsating microflows depends on its deformation type. For example, the lateral extension of an originally biconcave RBC becomes smaller in a Poiseuille flow. In contrast, the vertical extension increases for capsules or HeLa cells in Ref. [64]. The advance step has the opposite sign but particles of different elasticity are separated in both cases.

The presented generic propulsion phenomenon is independent on specific elastic properties of soft particles. Another great advantage of the method is that even cells with small elasticity differences can be separated by increasing the number of forward/reverse flow cycles. Furthermore, the oscillating fluid motion allows an efficient particle separation even in short channels compared to other methods. Since the suggested particle propulsion mechanism operates in the range of small Reynolds numbers (and thus small flow amplitudes), even larger bioparticles such as circulating tumor cells can be sorted at physiological shear stresses without the cells being damaged or showing a flow-induced response.

Our robust and label-free method fulfills a great need for separating cells with different mechanical properties, e.g., malignant cells and their healthy counterparts. Assuming RBCs of size $d_0 = 8 \mu\text{m}$ with a shear modulus κ_S of $7 \mu\text{Nm}^{-1}$ for healthy cells and $10 \mu\text{Nm}^{-1}$ for RBCs with the sickle cell mutation [15,68], we can approximate their different net progress. After 250 s of oscillation with a flow amplitude of $u_1 = 4.8 \text{ mm s}^{-1}$ and a flow asymmetry of 4 in a microchannel with height $2w = 21 \mu\text{m}$, healthy RBCs will have moved 3.6 mm, malignant cells only by 1.3 mm on average.

We gratefully acknowledge discussions with P.-Y. Gires, S.W. Krauss, and M. Weiss. For support, W.S. thanks the DAAD, W.S. and W.Z. thank the Elite Study Program Biological Physics, and all the authors thank the French-German University (Grant No. CFDA-Q1-14, Living fluids).

-
- [1] W. Lee, P. Tseng, and D. Di Carlo, Editors, *Microtechnology for Cell Manipulation and Sorting* (Springer, Cham, Switzerland, 2017).
 - [2] N.-T. Nguyen, S. T. Wereley, and S. A. M. Shaegh, *Fundamentals and Applications of Microfluidics* (Artech House, Boston, 2019).
 - [3] A. A. S. Bhagat, H. Bow, H. W. Hou, S. J. Tan, J. Han, and C. T. Lim, Microfluidics for cell separation, *Med. Biol. Eng. Comput.* **48**, 999 (2010).
 - [4] A. Karimi, S. Yazdi, and A. M. Ardekani, Hydrodynamic mechanisms of cell and particle trapping in microfluidics, *Biomicrofluidics* **7**, 021501 (2013).

- [5] P. Sajeesh and A. K. Sen, Particle separation and sorting in microfluidic devices: a review, *Microfluid Nanofluid* **17**, 1 (2014).
- [6] C. W. Shields IV, C. D. Reyes, and G. P. López, Microfluidic cell sorting: A review of the advances in the separation of cells from debulking to rare cell isolation, *Lab Chip* **15**, 1230 (2015).
- [7] J. B. Dahl, J.-M. G. Lin, S. J. Muller, and S. Kumar, Microfluidic strategies for understanding the mechanics of cells and cell-mimetic systems, *Annu. Rev. Chem. Biomol. Eng.* **6**, 293 (2015).
- [8] G.-H. Lee, S.-H. Kim, K. Ahn, S.-H. Lee, and J. Y. Park, Separation and sorting of cells in microsystems using physical principles, *J. Micromech. Microeng.* **26**, 013003 (2016).
- [9] D. Stoecklein and D. Di Carlo, Nonlinear Microfluidics, *Anal. Chem.* **91**, 296 (2019).
- [10] R. Nasiri, A. Shamloo, S. Ahadian, L. Amirifar, J. Akbari, M. J. Goudie, K. Lee N. Ashammakhi, M. R. Dokmeci, D. DiCarlo, and A. Khademhosseini, Microfluidic-based approaches and targeted cell/particle separation based on physical properties: Fundamentals and applications, *Small* **16**, 2000171 (2020).
- [11] S. Zhang, Y. Wang, P. Onck, and J. den Toonder, A concise review of microfluidic particle manipulation methods, *Microfluid Nanofluid* **24**, 24 (2020).
- [12] Z. Lin, G. Luo, W. Du, T. Kong, C. Liu, and Z. Liu, Recent advances in microfluidic platforms applied in cancer metastasis: Circulating tumor cells' (CTCs) isolation and tumor-on-a-chip, *Small* **16**, 1903899 (2020).
- [13] S. Suresh, Biomechanics and biophysics of cancer cells, *Acta Biomater.* **3**, 413 (2007).
- [14] J. Guck *et al.*, Optical deformability as an inherent cell marker for testing malignant transformation and metastatic competence, *Biophys. J.* **88**, 3689 (2005).
- [15] M. M. Brandão, A. Fontes, M. L. Barjas-Castro, L. C. Barbosa, F. F. Costa, C. L. Cesar, and S. T. O. Saad, Optical tweezers for measuring red blood cell elasticity: Application to the study of drug response in sickle cell disease, *Eur. J. Haematol.* **70**, 207 (2003).
- [16] E. M. Drost and W. MacNee, Potential role of IL-8, platelet-activating factor and TNF- α in the sequestration of neutrophils in the lung: effects of neutrophil deformability, adhesion receptor expression, and chemotaxis, *Eur. J. Immunol.* **32**, 393 (2002).
- [17] A. M. Dondorp, P. A. Kager, J. Vreeken, and N. J. White, Abnormal blood flow and red blood cell deformability in severe malaria, *Parasitol. Today* **16**, 228 (2000).
- [18] D. E. McMillan, N. G. Utterback, and J. La Puma, Reduced erythrocyte deformability in diabetes, *Diabetes* **27**, 895 (1978).
- [19] N. Debnath and M. Sadrzadeh, Microfluidic mimic for colloid membrane filtration: A Review, *J. Indian Inst. Sci.* **98**, 137 (2018).
- [20] J. Zhang, S. Yan, D. Yuan, G. Alici, N.-T. Nguyen, M. E. Warkiani, and W. Li, Fundamentals and applications of inertial microfluidics: a review, *Lab Chip* **16**, 10 (2016).
- [21] L. R. Huang, E. C. Cox, R. H. Austin, and J. C. Sturm, Continuous particle separation through deterministic lateral displacement, *Science* **304**, 987 (2004).
- [22] D. W. Inglis, J. A. Davis, R. H. Austin, and J. C. Sturm, Critical particle size for fractionation by deterministic lateral displacement, *Lab Chip* **6**, 655 (2006).
- [23] J. McGrath, M. Jimenez, and H. Bridle, Deterministic lateral displacement for particle separation: A review, *Lab Chip* **14**, 4139 (2014).
- [24] A. Hochstetter *et al.*, Deterministic lateral displacement: Challenges and perspectives, *ACS Nano* **14**, 10784 (2020).
- [25] Z. Zhang, W. Chien, E. Henry, D. A. Fedosov, and G. Gompper, Sharp-edged geometric obstacles in microfluidics promote deformability-based sorting of cells, *Phys. Rev. Fluids* **4**, 024201 (2019).
- [26] T. W. Secomb, Blood flow in microcirculation, *Annu. Rev. Fluid Mech.* **49**, 443 (2017).
- [27] I. Cantat and C. Misbah, Lift Force and Dynamical Unbinding of Adhering Vesicles under Shear Flow, *Phys. Rev. Lett.* **83**, 880 (1999).
- [28] U. Seifert, Hydrodynamic Lift on Bound Vesicles, *Phys. Rev. Lett.* **83**, 876 (1999).
- [29] M. Abkarian, C. Lartigue, and A. Viallat, Tank Treading and Unbinding of Deformable Vesicles in Shear Flow: Determination of the Lift Force, *Phys. Rev. Lett.* **88**, 068103 (2002).
- [30] L. G. Leal, Particle motions in a viscous fluid, *Annu. Rev. Fluid Mech.* **12**, 435 (1980).

- [31] S. Mandal, A. Bandopadhyay, and S. Chakraborty, Effect of interfacial slip on the cross-stream migration of a drop in an unbounded Poiseuille flow, *Phys. Rev. E* **92**, 023002 (2015).
- [32] B. Kaoui, G. H. Ristow, I. Cantat, C. Misbah, and W. Zimmermann, Lateral migration of a two-dimensional vesicle in unbounded Poiseuille flow, *Phys. Rev. E* **77**, 021903 (2008).
- [33] G. Coupier, B. Kaoui, T. Podgorski, and C. Misbah, Noninertial lateral migration of vesicles in bounded Poiseuille flow, *Phys. Fluids* **20**, 111702 (2008).
- [34] S. K. Doddi and P. Bagchi, Lateral migration of a capsule in a plane Poiseuille flow in a channel, *Int. J. Multiphase Flow* **34**, 966 (2008).
- [35] A. Farutin and C. Misbah, Symmetry breaking and cross-streamline migration of three-dimensional vesicles in an axial Poiseuille flow, *Phys. Rev. E* **89**, 042709 (2014).
- [36] A. Förtsch, M. Laumann, D. Kienle, and W. Zimmermann, Migration reversal of soft particles in vertical flows, *Europhys. Lett.* **119**, 64003 (2017).
- [37] M. Laumann, W. Schmidt, A. Farutin, D. Kienle, S. Förster, C. Misbah, and W. Zimmermann, Emerging Attractor in Wavy Poiseuille Flows Triggers Sorting of Biological Cells, *Phys. Rev. Lett.* **122**, 128002 (2019).
- [38] B. Dincau, E. Dressaire, and A. Sauret, Pulsatile flow in microfluidic systems, *Small* **16**, 1904032 (2020).
- [39] A. Lafzi, A. H. Raffiee, and S. Dabiri, Inertial migration of a deformable capsule in an oscillatory flow in a microchannel, *Phys. Rev. E* **102**, 063110 (2020).
- [40] S. M. Recktenwald, C. Wagner, and T. John, Optimizing pressure-driven pulsatile flows in microfluidic devices, *Lab Chip* **21**, 2605 (2021).
- [41] K. Loutherbach, J. Puchalla, R. H. Austin, and J. C. Sturm, Deterministic Microfluidic Ratchet, *Phys. Rev. Lett.* **102**, 045301 (2009).
- [42] S. M. McFaul, B. K. Lin, and H. Ma, Cell separation based on size and deformability using microfluidic funnel ratchets, *Lab Chip* **12**, 2369 (2012).
- [43] E. S. Park *et al.*, Continuous flow deformability-based separation of circulating tumor cells using microfluidic ratchets, *Small* **12**, 1909 (2016).
- [44] I. Jo, Y. Huang, W. Zimmermann, and E. Kalso, Passive swimming in viscous oscillatory flows, *Phys. Rev. E* **94**, 063116 (2016).
- [45] M. Laumann, P. Bauknecht, S. Gekle, D. Kienle, and W. Zimmermann, Cross-stream migration of asymmetric particles driven by oscillating shear, *Europhys. Lett.* **117**, 44001 (2017).
- [46] T. Morita, T. Omori, and T. Ishikawa, Passive swimming of a microcapsule in vertical fluid oscillation, *Phys. Rev. E* **98**, 023108 (2018).
- [47] B. R. Mutlu, J. F. Edd, and M. Toner, Oscillatory inertial focusing in infinite microchannels, *Proc. Natl. Acad. Sci. U.S.A.* **115**, 7682 (2018).
- [48] M. Laumann, A. Förtsch, E. Kalso, and W. Zimmermann, Engineering microswimmers by shaking liquids, *New J. Phys.* **21**, 073012 (2019).
- [49] J. Hendricks, T. Kawakatsu, K. Kawasaki, and W. Zimmermann, Confined semiflexible polymer chains, *Phys. Rev. E* **51**, 2658 (1995).
- [50] D. Barthès-Biesel, Motion and deformation of elastic capsules and vesicles in flow, *Annu. Rev. Fluid Mech.* **48**, 25 (2016).
- [51] G. Gompper and D.M. Kroll, Random surface discretizations and the renormalization of the bending rigidity, *J. Phys. I France* **6**, 1305 (1996).
- [52] T. Krüger, M. Gross, D. Raabe, and F. Varnik, Crossover from tumbling to tank-treading-like motion in dense simulated suspensions of red blood cells, *Soft Matter* **9**, 9008 (2013).
- [53] J. K. G. Dhont, *An Introduction to Dynamics of Colloids* (Elsevier, Amsterdam, 1996).
- [54] J. Rotne and S. Prager, Variational treatment of hydrodynamic interaction in polymers, *J. Chem. Phys.* **50**, 4831 (1969).
- [55] E. Wajnryb, K. A. Mizerski, P. J. Zuk, and P. Szymczak, Generalization of the Rotne-Prager-Yamakawa mobility and shear disturbance tensors, *J. Fluid Mech.* **731**, R3 (2013).
- [56] R. P. Zarda R. Skalak, A. Tozeren, and S. Chien, Strain energy function of red blood cell membranes, *Biophys. J.* **13**, 245 (1973).

- [57] M. Meyer, M. Desbrun, P. Schröder, and A. H. Barr, Discrete differential-geometry operators for triangulated 2-manifolds, in *Visualization and Mathematics III*, edited by H. C. Hege and K. Polthier (Springer, Berlin, 2003), p. 35.
- [58] C. S. Peskin, The immersed boundary method, *Acta Numerica* **11**, 479 (2002).
- [59] T. Krüger, F. Varnik, and D. Raabe, Efficient and accurate simulations of deformable particles immersed in a fluid using a combined immersed boundary lattice Boltzmann finite element method, *Comput. Math. Appl.* **61**, 3485 (2011).
- [60] T. Krüger, H. Kusumaatmaja, A. Kuzmin, O. Shardt, G. Silva, and E. M. Viggen, *The Lattice Boltzmann Method: Principles and Practice* (Springer, Berlin, 2016).
- [61] See Supplemental Material at <http://link.aps.org/supplemental/10.1103/PhysRevFluids.7.L032201> for a LBM simulation of multiple RBCs, a detailed description of the two simulation methods, the particle models, and the analytical calculation for the net progress of the minimal model.
- [62] Parameters for the MM: $\eta = 1$, $u_1 = 40$, $u_2 = -20$, $a = 0.1$, $b = 2$, $d = 3$, $k = 60$; simulation only: time step $\delta t = 2 \times 10^{-5}$, $T_1 = 0.6$, $T_2 = 1.2$, run time $t_{\text{end}} = 10(T_1 + T_2)$. Parameters for the ring polymer: $\delta t = 2 \times 10^{-4}$, $\eta = 1$, $a = 0.1$, $r_0 = 3$, $k = 10$, $\kappa = 50$, $w = 6$, $u_1 = 30$, $u_2 = -15$, $T_1 = 10$, $T_2 = 20$, $t_{\text{end}} = 5 \times (T_1 + T_2)$. Parameters for the capsule: $\delta t = 5 \times 10^{-2}$, $\eta = 1$, $a = 0.2$, initial edge length of one triangle $b = 1$ ($r_0 = 6.63$), $\kappa_S = 0.2$, $\kappa_B = 0.1$, $\kappa_V = 3$, $w = 20$, $u_1 = 1.5$, $u_2 = -0.75$, $T_1 = 1250$, $T_2 = 2500$, $t_{\text{end}} = 10 \times (T_1 + T_2)$. Parameters for the RBC: lattice constant $\delta x = 1$, $\delta t = 1$, LBM relaxation time $\tau = 1$, fluid density $\rho = 1$ ($\eta = 1/6$), $r_0 = 9$, system size in the y direction $2w = 47$, system size in the x and z directions (periodic boundaries) $S_x = S_z = 128$, $\kappa_S = 6.51879 \times 10^{-4}$, $\kappa_\alpha = 6.51879 \times 10^{-2}$, $\kappa_B = 2.08293 \times 10^{-4}$, $\kappa_V = 6.51879 \times 10^{-2}$, $u_1 = 1.6 \times 10^{-3}$, $u_2 = -4 \times 10^{-4}$, $T_1 = 2 \times 10^5$, $T_2 = 8 \times 10^5$, $t_{\text{end}} = 3 \times (T_1 + T_2)$.
- [63] A. Guckenberger, A. Kihm, T. John, C. Wagner, and S. Gekle, Numerical–experimental observation of shape bistability of red blood cells flowing in a microchannel, *Soft Matter* **14**, 2032 (2018).
- [64] O. Otto *et al.*, Real time deformability cytometry: On-the-fly cell mechanical phenotyping, *Nat. Methods* **12**, 199 (2015).
- [65] A. Mietke, O. Otto, S. Girardo, P. Rosendahl, A. Taubenberger, S. Golfier, E. Ulbricht, S. Aland, J. Guck, and E. Fischer-Friedrich, Real time deformability cytometry: On-the-fly cell mechanical phenotyping, *Biophys. J.* **109**, 2023 (2015).
- [66] M. M. Villone, F. Greco, M. A. Hulsen, and P. L. Maffettone, Numerical simulations of deformable particle lateral migration in tube flow of Newtonian and viscoelastic media, *J. Non-Newtonian Fluid Mech.* **234**, 105 (2016).
- [67] S. W. Krauss, P.-Y. Gires and M. Weiss, Deformation-induced actuation of cells in asymmetric periodic flow fields, doi: <https://doi.org/10.1101/2021.09.30.462560>.
- [68] S. Suresh, Mechanical response of human red blood cells in health and disease: Some structure-property-function relationships, *J. Mater. Res.* **21**, 1871 (2006).